Applied Catalysis B: Environment and Energy 351 (2024) 123993

Contents lists available at ScienceDirect

Applied Catalysis B: Environment and Energy

journal homepage: www.elsevier.com/locate/apcatb

Construction of carbonized polymer dots/potassium doped carbon nitride nanosheets Van der Waals heterojunction by ball milling method for facilitating photocatalytic CO_2 reduction performance in pure water

Jintao Dong [a], Junze Zhao [a], Xingwang Yan [b], Lina Li [a], Gaopeng Liu [b], Mengxia Ji [b], Bin Wang [a], Yuanbin She [c,*], Huaming Li [b], Jiexiang Xia [a,*]

[a] School of Chemistry and Chemical Engineering, Jiangsu University, Zhenjiang 212013, China
[b] Institute for Energy Research, Jiangsu University, Zhenjiang 212013, China
[c] State Key Laboratory Breeding Base of Green Chemistry-Synthesis Technology, College of Chemical Engineering, Zhejiang University of Technology, Hangzhou 310014, China

ARTICLE INFO

Keywords:
Carbon nitride
CO_2
Carbonized polymer dots
Van der Waals heterojunction
Photocatalysis

ABSTRACT

When the advancement of conventional heterojunctions is restricted by lattice matching of materials, Van der Waals heterojunctions formed by interlayer Van der Waals force present enormous development prospects with the revolution of graphene and graphene-like materials. Ascribed to similar graphene-like structures, carbonized polymer dots (CPDs) and potassium-doped carbon nitride nanosheets (KCNNS) were stacked by the ball milling method to form a novel Van der Waals heterojunction. Experimental analysis and density functional theory (DFT) calculations demonstrate that the constructed CPDs/KCNNS heterojunctions can effectively suppress sluggish reaction dynamics. CPDs/KCNNS-2 composites demonstrate enhanced CO_2 photoreduction performance (78.98 μmol g^{-1}•h^{-1}) with 100% CO selectivity in pure water, which is 13.71 times higher than that of KCNNS. *In-situ* FT-IR spectra were employed to identify the intermediates formed in the CO evolution process of CPDs/KCNNS composites. The manuscript provides a scientific reference for the stacking of Van der Waals heterojunction based on C_3N_4 in the artificial photosynthesis field.

1. Introduction

The large-scale production and utilization of fossil energy have promoted rapid economic development and enhanced living standards but led to massive CO_2 emissions, fossil energy exhaustion, and ecological imbalance [1,2]. The WMO organization published many related reports for the tempestuous change of the ecological environment ascribed to the unprecedented concentration levels of CO_2 (exceed 400 ppm) and the alarming ascent rate of CO_2 concentration [3,4]. Various strategies are employed for the reduction of CO_2 formation and emission, such as efficient utilization of fossil energy, the development and utilization of clean energy, and CO_2 capture, utilization, and storage (CCUS) technology. CCUS technology is regarded as a vital pathway for achieving the net-zero emission of CO_2 [5,6]. Among them, CO_2 also can be utilized as a non-toxic C1 feedstock to achieve the efficient conversion of CO_2 into valuable substances or products [7,8]. Inspired by plant photosynthesis, the artificial photosynthesis method has been developed to convert CO_2 into fuels and industrial raw materials driven by sunlight, which achieves successful conversion of solar energy to chemical energy [9,10]. The photocatalytic CO_2 reduction process butters both sides of one's bread attributed to the simultaneous CO_2 emission reduction and clean energy production [11,12]. However, the development of photocatalytic CO_2 reduction reaction is severely limited by the difficult activation of CO_2 on the photocatalysts ascribed to high C═O bond breaking energy (750 kJ mol^{-1}) and sluggish kinetics of electron transfer [9,12–14]. Therefore, the design and application of photocatalysts with high CO_2 activation and electron migration efficiency are of practical significance for accelerating the CO_2 photoreduction process.

The construction of heterojunctions exhibits great prospects in the CO_2 photoconversion field, which ascribes to the feasibility and universality of constructed heterojunctions for facilitating spatial separation of photogenerated carriers. In the initial research, the conventional heterojunctions were mainly composed of lattice-matched semiconductor materials, such as ion exchange reaction [15], *in-situ* epitaxial

* Corresponding authors.
E-mail addresses: sheyb@zjut.edu.cn (Y. She), xjx@ujs.edu.cn (J. Xia).

https://doi.org/10.1016/j.apcatb.2024.123993
Received 27 January 2024; Received in revised form 14 March 2024; Accepted 20 March 2024
Available online 21 March 2024

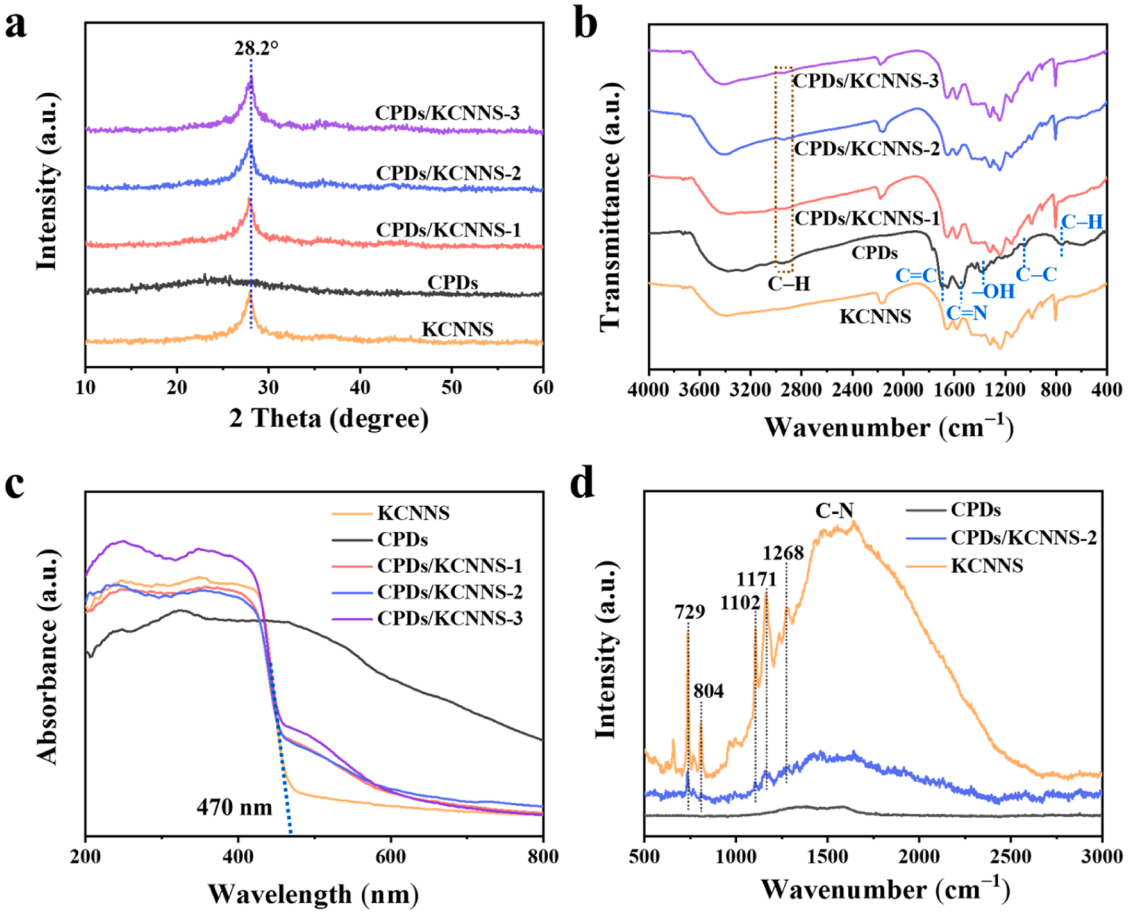

Fig. 1. (a) XRD patterns, (b) FT-IR spectra, and (c) UV-Vis DRS spectra of CPDs, pristine KCNNS, and CPDs/KCNNS-x composites; (d) Raman spectra of CPDs, pristine KCNNS and CPDs/KCNNS-2 composites.

growth on the matrix material [16], and heteroatom doping into intrinsic semiconductors [17]. However, the extensive use of heterojunctions is severely restricted by the harsh requirements of traditional heterojunctions for lattice matching and the formation of unsaturated dangling bonds in the construction process [18]. Simultaneously, with the continuous development of two-dimensional (2D) graphene-like atomic materials without hanging bonds, various 2D atomic-layer materials are stacked by weak Van der Waals forces to construct new-type Van der Waals heterojunctions with flat interfaces [19,20]. Significantly, the construction of the Van der Waals heterojunction would not destroy the structure and performance of components, and provides a great possibility for integrating various 2D materials, laying the solid material foundation for the nano-electronic and nano-optoelectronics field [21,22]. Consequently, the construction of Van der Waals heterojunctions has also become an emerging research hotspot in the design and integration of high-performance photocatalysts for CO_2 reduction [18,23,24]

Carbon nitride (C_3N_4) is a typical 2D polymer semiconductor with graphene-like structures by sp^2 hybridization of N and C atoms. Ascribed to the characteristic physicochemical property and adjustable band structure, C_3N_4 is supposed to be a suitable candidate for the construction of Van der Waals heterojunction to accelerate photoinduced electron separation [18,25]. Various C_3N_4-based Van der Waals heterojunction photocatalysts were employed in the photocatalytic CO_2 reduction process, such as FLI_2/KCNNS [26], Sb/g-C_3N_4 [27], Co-rGO/C_3N_4 [28], et al. The structure of carbonized polymer dots (CPDs) is a hybrid structure composed of highly cross-linked or graphitized carbon core and external polymer chains with hydrophilic groups [29,30]. CPDs are prepared through dehydration, condensation, cross-linking, and carbonization processes with polymers or organic molecules. Additionally, as rapidly developing carbon-based nanoparticles, CPDs also exhibit the prominent application prospect for photocatalytic conversion of CO_2 ascribed to low toxicity, favorable conductivity, exceptional quantum yield, and satisfactory stability [31]. The CPDs/$Bi_4O_5Br_2$ heterojunction prepared by Wang et al. realized the enhancement of photoinduced electron transfer and separation ability to obtain superior photocatalytic CO evolution performance [32]. Cao's group reported that the introduction of CPDs successfully achieved photogenerated electron transfer of CPDs/BiOBr heterojunction in favor of CO_2 conversion [33]. Consequently, CPDs can be perceived as potential alternatives for coupling with C_3N_4 to construct Van der Waals heterojunction with satisfactory photocatalytic CO_2 reduction performance.

Herein, carbonized polymer dots/potassium-doped carbon nitride nanosheets (CPDs/KCNNS) Van der Waals heterojunction was successfully constructed by the ball milling method. CPDs/KCNNS composites would achieve remarkable enhancement of photogenerated electron separation efficiency ascribed to the construction of Van der Waals heterojunction. Additionally, CPDs/KCNNS composites also can strengthen CO_2 absorption and light utilization ascribed to the introduction of CPDs. Consequently, without cocatalysts, hole scavengers, and organic solvents, CPDs/KCNNS-2 composites possess an exceptional CO generation rate (78.98 μmol g^{-1}•h^{-1}) with a 0.86% apparent quantum yield at 400 nm in pure water, which is 13.71 times higher than that of pristine KCNNS. The manuscript provides an instructive reference for constructing C_3N_4-based Van der Waals heterojunction by the ball milling method, actualizing large-scale applications of artificial photosynthesis.

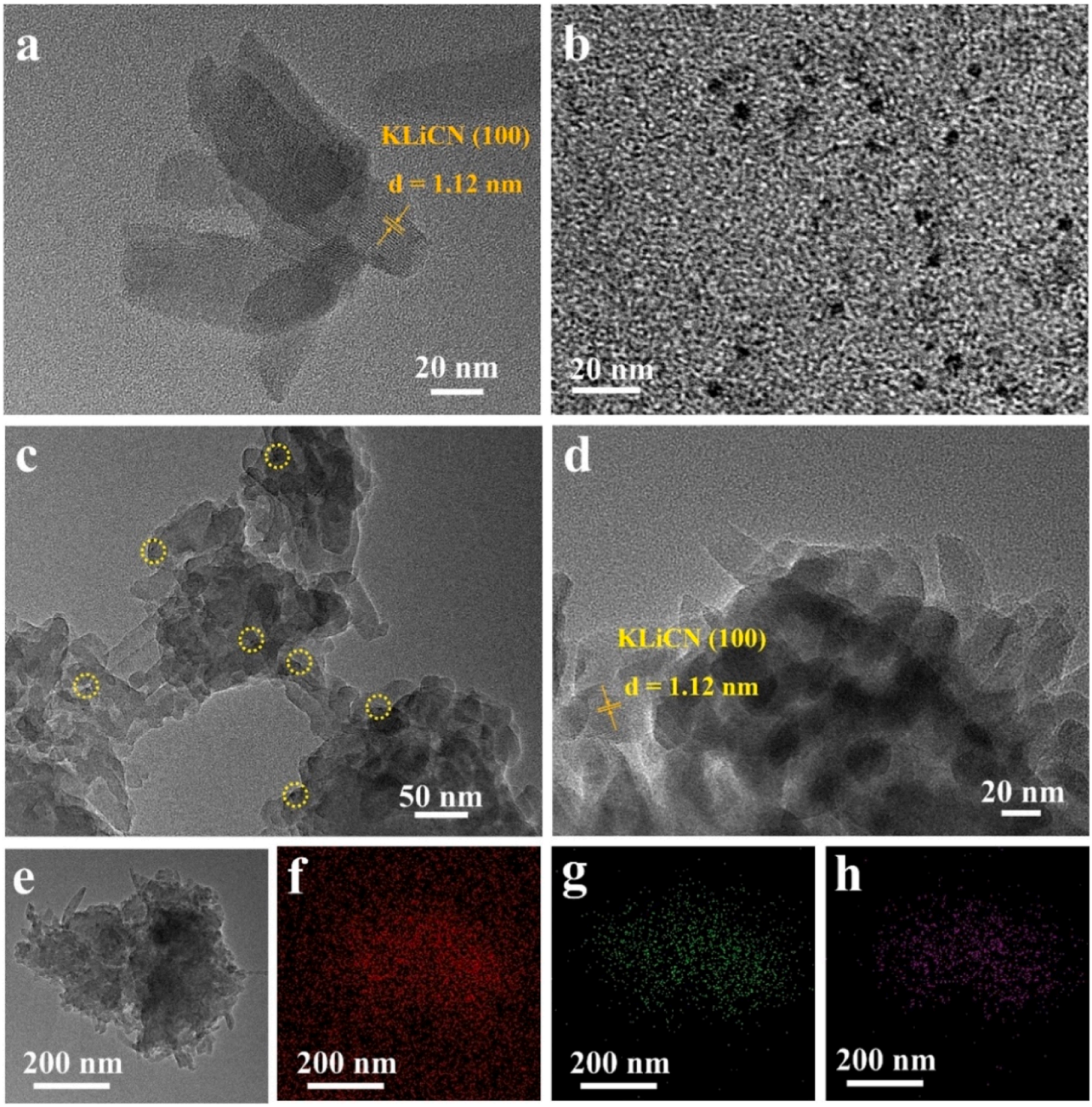

Fig. 2. TEM images of (a) pristine KCNNS, (b) CPDs, and (c-e) CPDs/KCNNS-2 composites; the corresponding mapping images (f-h) of C, N, K elements in CPDs/KCNNS-2 composites.

2. Experimental section

2.1. Experimental reagents

The chemicals melamine (CP), KCl (GR), LiCl (99.0%), EtOH (AR), citric acid (AR), and ethylenediamine (AR) were acquired from Sinopharm Chemical Reagent Co., Ltd.

2.2. Synthesis of photocatalysts

Carbonized polymer dots (CPDs): Firstly, 5 mmol citric acid and 335 μL ethylenediamine were dispersed in 10 mL of deionized water. Subsequently, the solution was heated for 5 h at 200 °C in an oven to prepare brown CPDs dispersion. Finally, CPDs were extracted from the brown dispersion after 48 h dialysis and freeze-drying treatment.

Potassium-doped carbon nitride nanosheets (KCNNS): 10 g melamine was calcinated in the Muffle furnace at 550 ℃ for 4 h to obtain bulk C_3N_4. Subsequently, 5.5 g KCl, 1 g bulk C_3N_4, and 4.5 g LiCl were injected into a agate tank along with 10 bearing balls. The agate tank was attached to a high-energy ball milling device (MSK-SFM-3) for conducting a 30-min experiment at a revolution speed of 1200 rpm. After that, the mixtures obtained after ball milling were calcinated in the tubular furnace at 550 ℃ for 4 h under Ar condition. Finally, the products were washed with deionized water and anhydrous EtOH serval times and dried in a vacuum drying oven. The as-prepared material was named KCNNS.

Carbonized polymer dots/potassium-doped carbon nitride nanosheets (CPDs/KCNNS) composites: a certain amount of CPDs, 1 g KCNNS, and 1 mL ethanol were injected into an agate tank and carried out 120-min ball milling experiment at a revolution speed of 1200 rpm.

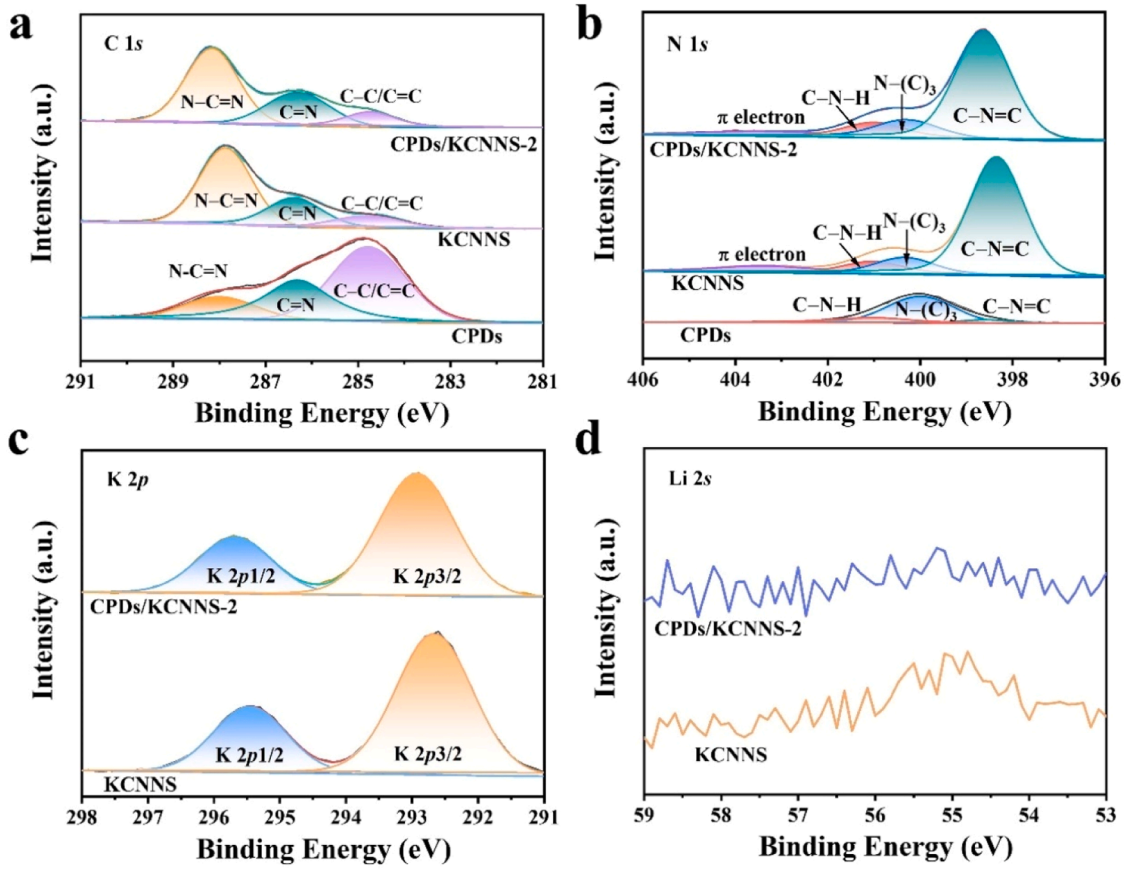

Fig. 3. The high-resolution XPS spectra of CPDs, pristine KCNNS, and CPDs/KCNNS-2 composites: (a) C 1 *s*, (b) N 1 *s*, (c) K 2*p*, and (d) Li 2 *s*.

The obtained products were dried in a vacuum drying oven. CPDs/KCNNS-1, CPDs/KCNNS-2, and CPDs/KCNNS-3 composites were prepared by the addition of 30, 50, and 70 mg CPDs.

2.3. Photocatalytic CO_2 reduction

The photocatalytic CO_2 reduction performance of CPDs, pristine KCNNS, and CPDs/KCNNS-x composites were carried out with a PLS-SXE300D Xenon lamp source and Labsolar-6A all glass automatic online trace gas analysis system (Beijing Perfectlight Technology Co., Ltd.) under a constant temperature (5 °C) for preventing thermocatalytic effects. Firstly, 30 mg photocatalysts and 50 mL deionized water were injected into a 350 mL silicon reactor. The evacuation process of the silicon reactor was carried out to remove air. Then, CO_2 (99.999%) was bubbled into the silicon reactor, and the system pressure was maintained at 80 kPa pressure. Eventually, the products of the photocatalytic CO_2 reduction process were determined by Zhejiang Fuli GC-9790II gas chromatography.

3. Result discussion

As illustrated in Fig. S1, the obvious diffraction peaks at about 13.1° and 27.3° of bulk C_3N_4 precursor match (100) and (002) faces, corresponding to intra-layer and inter-layer stacking, respectively [34]. It is noteworthy that the sharp diffraction peak at 13.0° disappears in the pristine KCNNS, which demonstrates the dimensions reduction of the intra-layer for pristine KCNNS. Significantly, the peak of (002) face shifts from 27.3° to 28.2°, and the peak intensity of (002) face for pristine KCNNS is obviously lower than that of bulk C_3N_4 precursor, which also implies the size miniaturization of inter-layer for pristine KCNNS [35]. As demonstrated in Fig. 1a, significant changes for a characteristic peak at 28.2° were not observed in CPDs/KCNNS-x composites compared with pristine KCNNS, indicating that the ball milling method has no significant impact on the crystal structure of CPDs/KCNNS-x composites. As observed in Fig. 1b, the distinct peaks located at 808 cm^{-1}, 1150–1650 cm^{-1}, and 2197 cm^{-1} in pristine KCNNS and CPDs/KCNNS-2 composites were perceived as out-of-plane bending vibration of the triazine ring, stretching vibration of conjugated C-N heterocycles, and C≡N bond [36]. Furthermore, various peaks situated at 761 cm^{-1}, 1052 cm^{-1}, 1379 cm^{-1}, 1552 cm^{-1}, 1697 cm^{-1} and 2945 cm^{-1} in CPDs individually match with the bending vibration of C–H, stretching vibration of C–C, in-plane stretching vibration of –OH, stretching vibration of C═N, C═C and C–H (Fig. 1b). Significantly, a weak C–H peak at 2945 cm^{-1} appears in CPDs/KCNNS-x composites, which demonstrates the successful formation of CPDs/KCNNS-x Van der Waals heterojunction. The absorption edge of pristine KCNNS is approximately 470 nm, and the obvious redshift was not observed in CPDs/KCNNS-x composites (Fig. 1c), implying that the construction of Van der Waals heterojunction has no significant influence on the structure of KCNNS. Significantly, an emerging absorption band between 470 nm and 580 nm was observed in CPDs/KCNNS-x composites, which demonstrates that CPDs/KCNNS Van der Waals heterojunction can efficiently exploit visible light. The empirical equation $\alpha h\nu = A\,(h\nu - E_g)^{n/2}$ is employed to calculate the band gap energy (E_g) of CPDs and KCNNS, where α, $h\nu$, E_g, and A parameters mean the absorption coefficient, photon energy, E_g, and constant, respectively. The E_g of CPDs and KCNNS is estimated as 2.59 and 1.56 eV (Fig. S4, S5). As demonstrated in Fig. 1d, the Raman band situated at 729, 804, 1102, 1171, 1268, and 1300–2100 cm^{-1} in KCNNS and CPDs/KCNNS-2 composites corresponding to the vibrational modes for N-breathing mode of triazine units and C–N heterocyclic rings, respectively [37].

Transmission electron microscope (TEM) measurement was

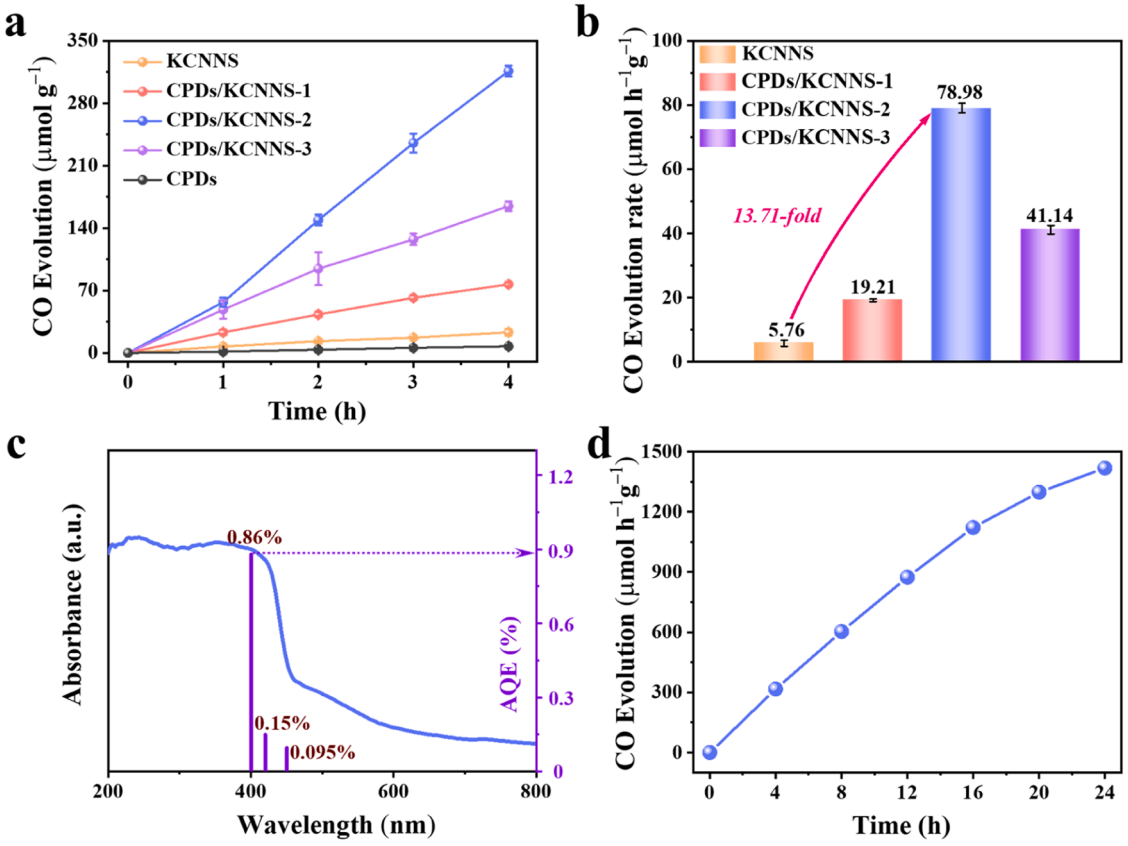

Fig. 4. (a) Time dependence of the CO product evolution for CPDs, pristine KCNNS, and CPDs/KCNNS composites; (b) the CO production rates of pristine KCNNS and CPDs/KCNNS composites under Xe lamp irradiation; (c) AQE of CPDs/KCNNS-2 composites at different wavelengths of monochromatic light overlaid with the light absorption curve of CPDs/KCNNS-2 composites; (d) the stability of CPDs/KCNNS-2 composites for photocatalytic CO_2 conversion.

employed to analyze the micromorphology of pristine KCNNS and CPDs/KCNNS-2 composites. As observed in Fig. 2a and Fig. 2c-e, pristine KCNNS and CPDs/KCNNS-2 composites also possess a nanosheet structure. The ordered lattice fringe with a spacing of 1.12 nm was observed in pristine KCNNS and CPDs/KCNNS-2 composites (Fig. 2a, d), which is responsible for the (100) plane of KCNNS [35]. The spherical CPDs have been observed in Fig. 2b. Many CPDs (in yellow circle) were also observed in CPDs/KCNNS-2 composites, which further certificates the stacking of CPDs and pristine KCNNS by ball milling method (Fig. 2c). The TEM image (Fig. 2e) and the corresponding mapping images (Fig. 2f-h) of CPDs/KCNNS-2 composites demonstrate C, N and K elements uniformly distributed in the surface of CPDs/KCNNS-2 composites.

X-ray photoelectron spectroscopy (XPS) characterization was employed to investigate compositions and elementary substances of CPDs, pristine KCNNS, and CPDs/KCNNS-x composites. The high-resolution C 1 *s* spectra of CPDs, pristine KCNNS, and CPDs/KCNNS-x composites (Fig. 3a) are Gaussian deconvoluted to three sharp peaks assigned to C–C/C═C, C═N, and N–C═N bonds [38]. As illustrated in Fig. 3b, three peaks for C–N═C, N–(C)$_3$, and C–N–H bonds of CPDs,

Table 1
Comparison of other C_3N_4-based materials for photocatalytic CO_2 reduction.

Photocatalyst	Catalyst Dosage (mg)	Light source	Performance (μmol g^{-1} h^{-1})	CO Selectivity	Ref.
BON/CN-2	20	300 W Xenon lamp	14.84	100%	[34]
CN-BiOBr-OV	10	300 W Xenon lamp	61.8	69.5%	[38]
Ni/S-CN-N	10	300 W Xenon lamp	11.72	75.6%	[39]
Cu1/N2CV-CN	5	300 W Xenon lamp	11.12	98.50%	[40]
BIF-20@g-C_3N_4	20	300 W Xenon lamp	53.869	77.60%	[42]
Cu_1N_3@PCN	10	300 W Xenon lamp	49.8	100%	[43]
HD-Er1/CN-NT	20	300 W Xenon lamp	47.1	95.0%	[44]
Mn_1Co_1/CN	50	300 W Xenon lamp	47.0	100%	[45]
Co_1Ag_1−PCN	10	300 W Xenon lamp	46.82	70.10%	[46]
SCC-2	50	300 W Xenon lamp	40.8	86.50%	[47]
CoRu-HCNp	25	300 W Xenon lamp	27.3	97.60%	[48]
α-Fe_2O_3/g-C_3N_4	25	300 W Xenon lamp	27.2	100%	[49]
0.7Ni-5OB-CN	100	300 W Xenon lamp	22.1	71.70%	[50]
FeN_4/K-g-C_3N_4	30	300 W Xenon lamp	20	99.60%	[51]
PtCu-crCN	25	300 W Xenon lamp	11.74	80.70%	[52]
Ni_5-CN	25	300 W Xenon lamp	8.6	88.10%	[53]
0.7 at% P-PCN	30	300 W Xenon lamp	5.37	83.0%	[54]
Cu-CCN	25	300 W Xenon lamp	3.086	100%	[54]
CPDs/KCNNS-2	**30**	**300 W Xenon lamp**	**78.98**	**100%**	**This work**

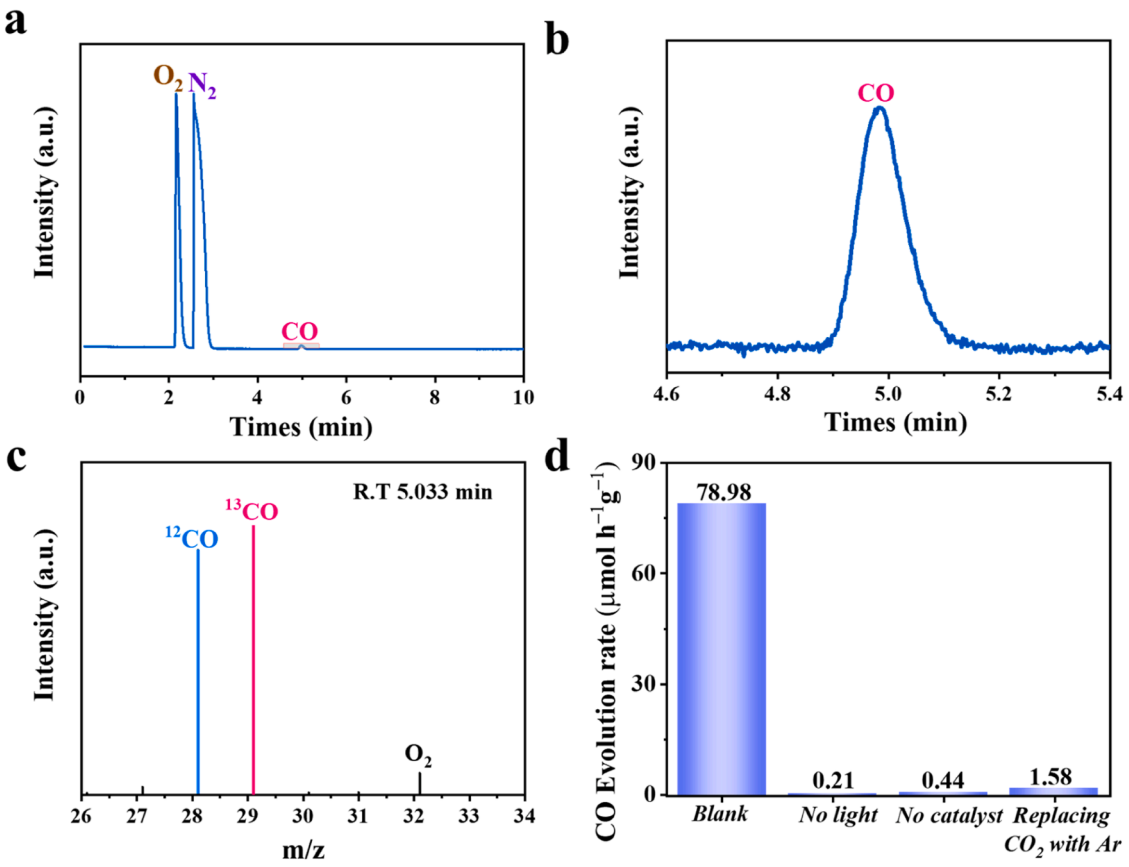

Fig. 5. (a) the total ion chromatograph and (b) partial enlargement of the total ion chromatograph for CPDs/KCNNS-2 composites in the photocatalytic $^{13}CO_2$ reduction process; (c) Mass spectra of ^{13}CO (m/z = 29) produced over CPDs/KCNNS-2 composites in the photocatalytic $^{13}CO_2$ reduction with CO_2 mixture gas (V($^{12}CO_2$): V($^{13}CO_2$) = 1: 1); (d) the average CO generation rates under multiple experiments of control conditions for CPDs/KCNNS-2 composites.

pristine KCNNS, and CPDs/KCNNS-2 composites were also observed in the N 1 *s* XPS spectra [38–40]. The aforementioned result indicates that CPDs and pristine KCNNS possess similar graphene-like structures contributing to the construction of Van der Waals heterojunction. Additionally, the high-resolution K 2*p* spectra (Fig. 3c) of pristine KCNNS and CPDs/KCNNS-2 composites are divided into two conspicuous peaks at 292.7 and 295.5 eV assigned to K 2*p*3/2 and K 2*p*1/2 orbits, which demonstrates that K^+ were embedded into high-crystallinity pristine KCNNS [35]. Simultaneously, the distinct peak disappears in the Li 1 *s* XPS spectra (Fig. 3d) of pristine KCNNS and CPDs/KCNNS-2 composites, implying the absolute removal of Li^+ in KCNNS and CPDs/KCNNS-2 composites.

For evaluating the impact of Van der Waals Heterojunction based on CPDs and pristine KCNNS, the photocatalytic CO evolution performance of CPDs, pristine KCNNS, and CPDs/KCNNS-x composites was measured in pure water without the injection of sacrificial agents and co-catalysts. As observed in Fig. 4a, CPDs and pristine KCNNS achieve a continuous photocatalytic CO generation with a rate of 1.85 and 5.76 μmol g^{-1} h^{-1}, demonstrating that CPDs and pristine KCNNS possess the intrinsic activity for photocatalytic CO_2 reduction. Ascribed to the construction of CPDs/KCNNS Van der Waals heterojunction, all the CPDs/KCNNS-x composites achieve a remarkable enhancement of CO_2 reduction activity compared with CPDs and pristine KCNNS. Furthermore, CPDs/KCNNS-2 composites exhibit the optimized CO evolution rate (Fig. 4b), affording a CO evolution rate of 78.98 μmol g^{-1}•h^{-1}, which enhances approximately 12.71 folds than that of pristine KCNNS. The photocatalytic CO_2 conversion measurements using a monochromic light source were carried out to show exceptional CO evolution characteristics under visible light (Fig. S8). With 400, 420, and 450 nm monochromic light irradiation, the CO evolution rate of CPDs/KCNNS-2 composites reach 45.61, 8.68, and 6.35 μmol g^{-1}•h^{-1}, respectively (Fig. S9). The optimized apparent quantum efficiency (AQE) value was revealed in the CPDs/KCNNS-2 composites (Fig. 4c) at a wavelength of 400 nm (0.86%), 420 nm (0.15%), 450 nm (0.095%), corresponding to the total utilization of excitation electrons [41]. The above-mentioned results further indicate the superior light conversion efficiency of CPDs/KCNNS-2 composites. The cycle stability is esteemed as an indispensable measurement factor for estimating the application value of photocatalysts. CPDs/KCNNS-2 composites exhibit sustainable 24 h CO evolution performance (Fig. 4d), demonstrating that CPDs/KCNNS-2 composites possess a promising prospect for large-scale industrialization. The distinct changes of the diffraction peaks (Fig. S10) and TEM image (Fig. S11) for CPDs/KCNNS-2 composites after cycle measurement were not observed compared with fresh CPDs/KCNNS-2 composites, which demonstrates that CPDs/KCNNS-2 composites possess satisfactory structural stability. Compared with the previous reports (Table 1) for C_3N_4-based materials [34,38–40,42–55], CPDs/KCNNS-2 composites simultaneously display higher CO selectivity (100%) and satisfactory CO evolution rate (78.98 μmol g^{-1}•h^{-1}), revealing the immense potential for the construction of Van der Waals heterojunction to achieve efficient artificial photosynthesis process with exceptional selectivity and activity.

Real carbon source tracking is a significant issue in effectively measuring the true activity of catalysts in CO_2 reduction reactions. The obvious chromatographic peak was observed in Fig. 5a-b, demonstrating that adding CO_2 in the photocatalytic CO_2 reduction reaction can be reduced to CO. The isotope tracer technique was carried out to further verify the carbon source in the photocatalytic CO_2 reduction process with CO_2 mixture gas (V($^{12}CO_2$): V($^{13}CO_2$) = 1: 1). The peaks at m/z = 28 and 29 in mass spectra correspond to ^{12}CO and ^{13}CO, further

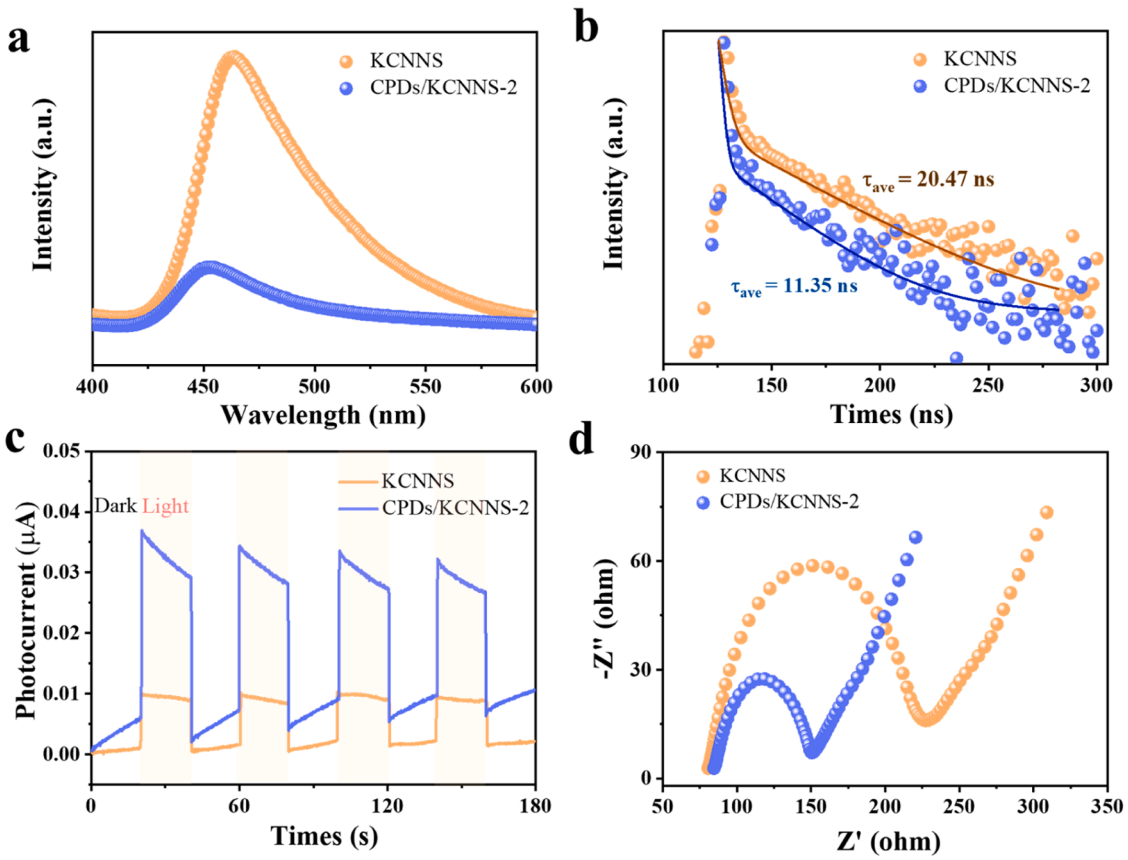

Fig. 6. (a) PL spectra, (b) PL delay spectra, (c) transient photocurrent response, and (d) EIS spectroscopy of pristine KCNNS and CPDs/KCNNS-2 composites.

illustrating carbon source originates from the injection of $^{12}CO_2$ and $^{13}CO_2$ (Fig. 5c) rather than carbon residue on the surface of CPDs/KCNNS-2 composites. As shown in Fig. 5d, illumination, CPDs/KCNNS-2 composites, and inpouring CO_2 are universal ingredients with the multivariable control system, inferring that inpouring CO_2 rather than surface-adsorbed carbon was reduced to CO.

The photogenerated carrier separation ability of photocatalysts is deemed a key factor for determining CO_2 reduction performance. Photoluminescence (PL) spectra illustrate that CPDs/KCNNS-2 composites possess lower peak intensity than that of pristine KCNNS (Fig. 6a), manifesting that the construction of CPDs/KCNNS-2 Van der Waals heterojunction contributes to decreasing recombination rate of photogenerated electron-hole pairs [56]. The transient PL decay spectra of pristine KCNNS and CPDs/KCNNS-2 composites were further investigated to determine the separation performance of photogenerated carriers. As illustrated in Fig. 6b, the average lifetime (τ_{ave}) of CPDs/KCNNS-2 composites (11.35 ns) is distinctly shorter than that of pristine KCNNS (20.47 ns), illustrating that CPDs/KCNNS-2 composites realize remarkably strengthened charge separation and migration efficiency [57]. The photoelectrochemical (PEC) tests of pristine KCNNS and CPDs/KCNNS-2 composites were performed to demonstrate efficient charge separation of CPDs/KCNNS-2 composites. CPDs/KCNNS-2 composites possess higher photocurrent response intensity compared with pristine KCNNS (Fig. 6c), which is attributed to the stacking of Van der Waals heterojunction for accelerating photoinduced carrier migration in the interface of CPDs/KCNNS-2 composites [45]. In contrast to pristine KCNNS, the smaller Nyquist radius arc is observed in CPDs/KCNNS-2 composites (Fig. 6d), further manifesting that the interface electronic transmission efficiency of CPDs/KCNNS-2 composites was significantly boosted.

As illustrated in the Mott-Schottky plot (Fig. S12-S13), the flat band potential (E_{flat}) of CPDs and pristine KCNNS was measured as –0.79 V and –0.56 V (vs NHE, pH = 7). CPDs and pristine KCNNS are identified as n-type semiconductors based on a positive slope of the Mott-Schottky plot. The conduction band position (E_{CB}) of CPDs and pristine KCNNS is approximately 0.1–0.3 eV below the E_{flat}, and 0.2 was selected as the value in the manuscript [58]. So, E_{CB} of CPDs and pristine KCNNS are reckoned as –0.99 eV and –0.76 eV. Consequently, the valence band potential (E_{VB}) of CPDs and pristine KCNNS is deduced as 0.57 eV and 1.83 eV by the equation ($E_g = E_{VB} - E_{CB}$), respectively [59].

For demonstrating electron direction in constructed CPDs/KCNNS heterojunction, the work function (Φ) of CPDs and pristine KCNNS is calculated by the DFT method, which can explore the energy difference between the Fermi level and vacuum level of CPDs and pristine KCNNS. As demonstrated in Fig. 7b, d and f, the Φ value of KCNNS (100) plane, CPDs (100) plane, and CPDs/KCNNS heterojunction are 4.08, 4.68, and 4.18 eV, respectively, revealing higher Fermi levels of KCNNS (100) plane than that of CPDs (100) plane and the Fermi level of the CPDs/KCNNS heterojunction is in the middle of CPDs and pristine KCNNS. Consequently, the mutual contact between CPDs and KCNNS brings about electron direction migration from KCNNS to CPDs, leading to band bending of CPDs and pristine KCNNS and achieving the balance of Fermi level. So, the built-in interface electric field forms in the contact interface between pristine KCNNS and CPDs (Fig. 8).

Except for the electron transfer process, the CO_2 adsorption capacity of photocatalysts is perceived as a constraint element affecting the CO_2 photoconversion ability. As illustrated in Fig. 9a, the maximum adsorption capacity of CPDs/KCNNS-2 composites reaches 9.22 cm^{-3} g^{-1}, which is 1.83 times than that of pristine KCNNS (5.03 cm^{-3} g^{-1}), thus facilitating the CO_2 adsorption performance of CPDs/KCNNS-2 composites to obtain superior CO_2 photoreduction performance. *In-situ* FT-IR spectra (Fig. 9b) were carried out to investigate the CO_2 conversion process for CPDs/KCNNS-2 composites. These distinct peaks match m-CO_3^{2-} (1291 cm^{-1}), b-CO_3^{2-} (1346 cm^{-1}), HCO_3^- (1465 cm^{-1}), COOH*

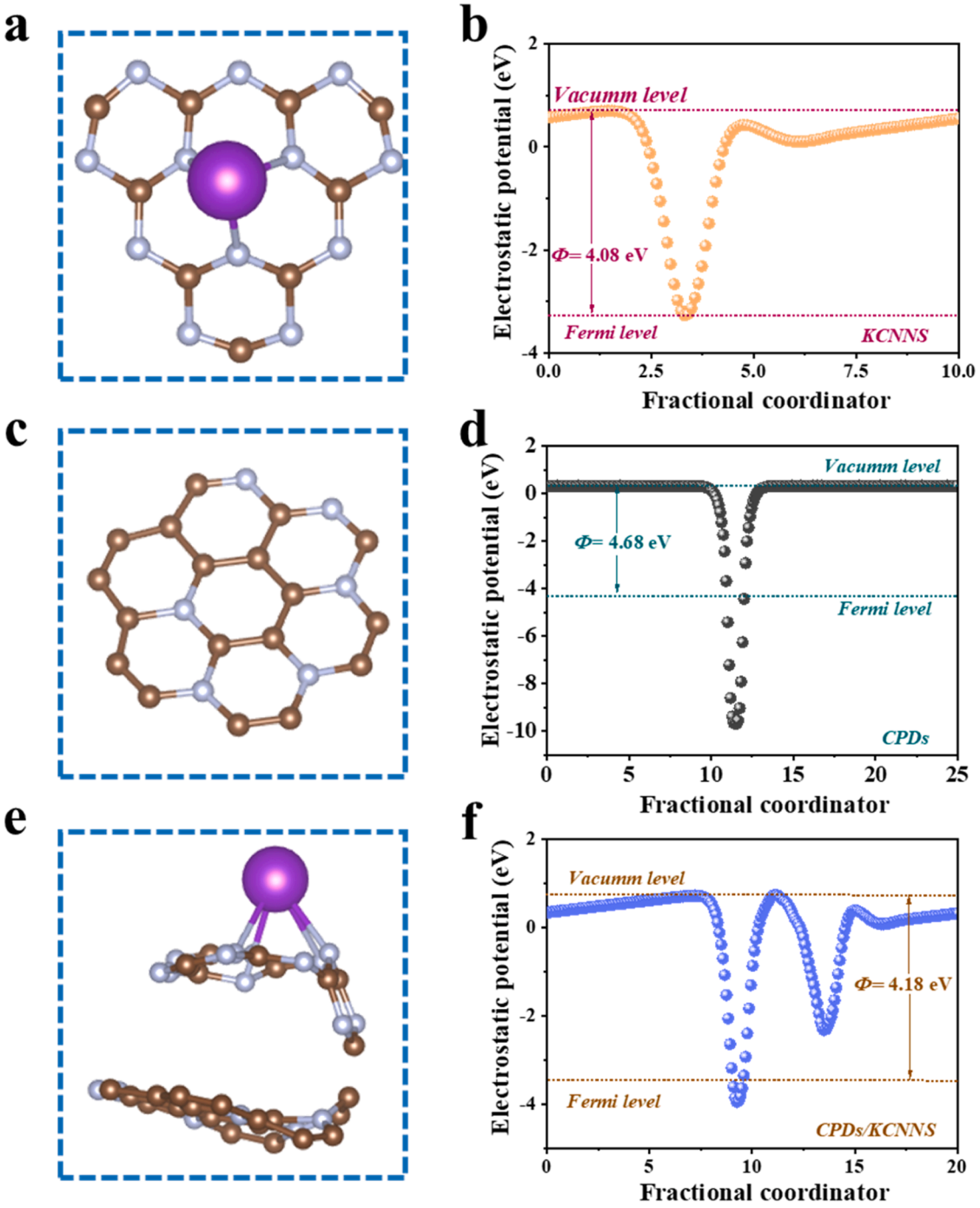

Fig. 7. The (a, c, e) corresponding structural model and (b, d, f) calculated work function for (100) plane of KCNNS, (100) plane of CPDs, and CPDs/KCNNS heterojunction.

(1551 cm^{-1}), $HCOO^-$ (1586 cm^{-1}) and CO_2^- (1727 cm^{-1}) and the peak intensity increase with illumination time extension [36,48,52,60]. Among them, COOH* is identified as a significant intermediate in the photocatalytic CO_2-to-CO conversion. So, the schematic mechanism of CPDs/KCNNS-2 composites for efficient CO_2 photoconversion is illustrated in Fig. 9c according to the multiple proton-couple electron migration processes [39,48,52]

The type II electron migration pathway based on CPDs and KCNNS is demonstrated in Fig. 10. CPDs are photoexcited by illumination, and the photoinduced electrons originating from the VB of CPDs migrate to the CB of CPDs. Subsequently, the photoelectrons would transfer from CPDs to KCNNS and CO_2 would be reduced to CO by the photoelectrons in CB of KCNNS ascribed to the more negative E_{CB} (–0.99 eV) of CPDs compared to that of KCNNS (–0.76 eV) and $E_{CO2/CO}$(–0.53 eV). Eventually, the holes remained on the VB of KCNNS transfers to the VB of CPDs. Consequently, the construction of CPDs/KCNNS Van der Waals heterojunction can facilitate electron migration efficiency contributing to advancing CO_2 photoconversion performance.

4. Conclusion

In summary, the CPDs/KCNNS Van der Waals heterojunction was successfully constructed by the stack of CPDs and KCNNS employing the ball milling method. Based on DFT calculation and experimental

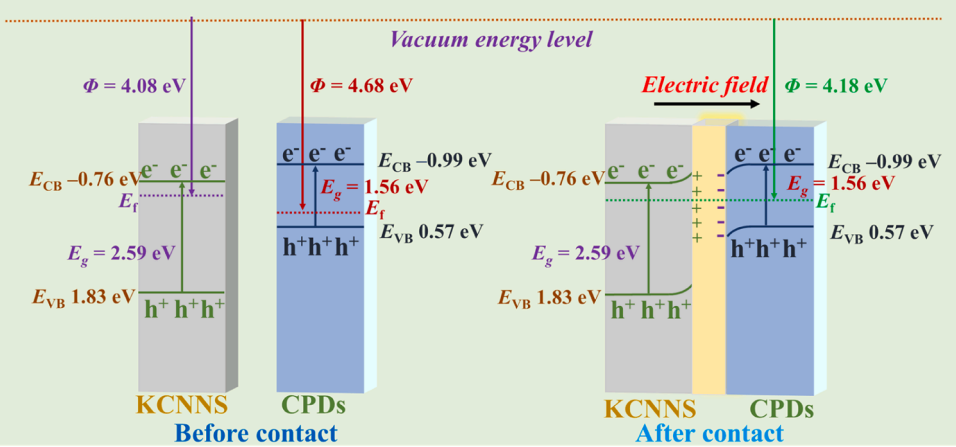

Fig. 8. The interfacial charge transfer between the CPDs and KCNNS in Van der Waals heterojunction.

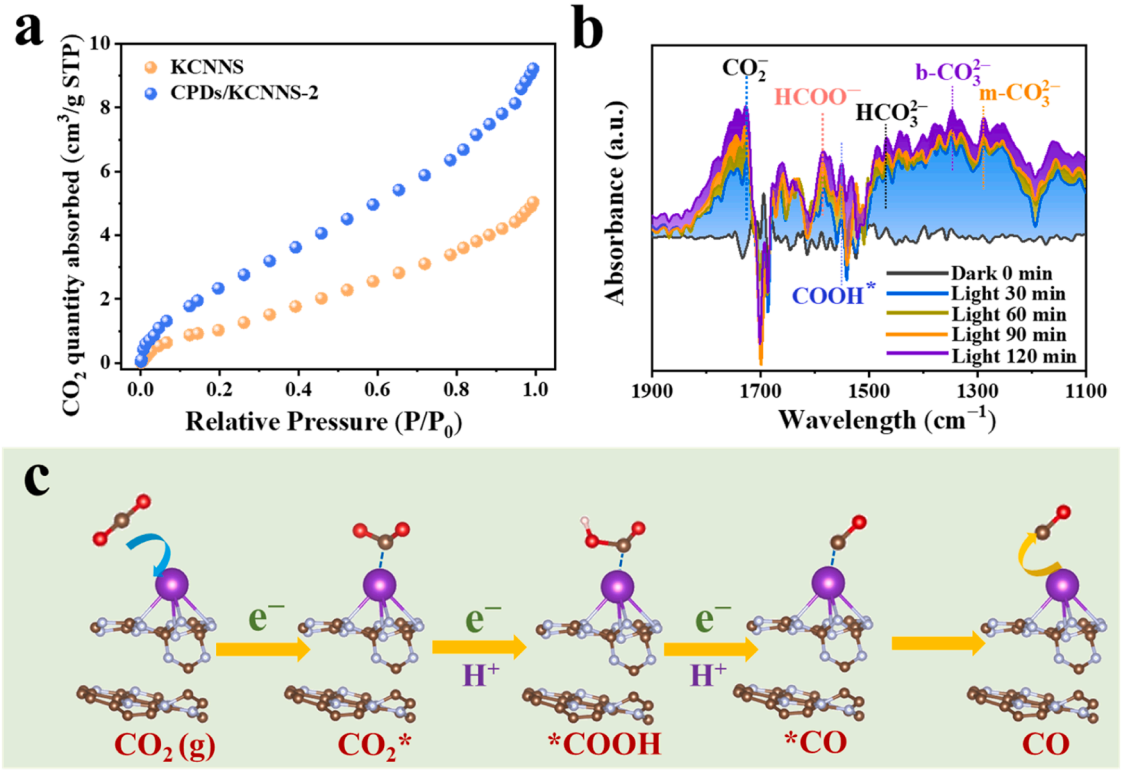

Fig. 9. (a) CO_2 adsorption curve of pristine KCNNS and CPDs/KCNNS-2 composites, (b) *in-situ* FTIR spectra of CPDs/KCNNS-2 composites in the CO_2 reduction process, (c) schematic mechanism of CPDs/KCNNS-2 composites for efficient CO_2 photoconversion.

characterization analysis, the introduction of CPDs markedly enhances CO_2 absorption, light utilization, and photogenerated electron separation efficiency of CPDs/KCNNS composites. CPDs/KCNNS-2 composites possess optimized CO evolution performance (78.98 μmol g^{-1}•h^{-1}) with 100% CO selectivity in pure water, which reaches 13.71 times higher than that of pristine KCNNS. Additionally, the CO evolution rate of CPDs/KCNNS-2 composites reaches 45.61 μmol g^{-1}•h^{-1}, 8.68 μmol g^{-1}•h^{-1}, and 6.35 μmol g^{-1}•h^{-1} under monochromic light irradiation (400, 420, and 450 nm), respectively. The intermediates formed in the CO_2 photoreduction process were analyzed by *In-situ* FT-IR spectra to propose the possible generation pathway. The manuscript provides a novel perspective for constructing high-performance C_3N_4-based material, broadening the application of Van der Waals heterojunctions in the field of photocatalytic CO_2 reduction.

CRediT authorship contribution statement

Gaopeng Liu: Resources, Investigation. **Mengxia Ji:** Software, Resources. **Xingwang Yan:** Visualization, Software, Resources. **Lina Li:** Validation, Software. **Jintao Dong:** Writing – original draft, Visualization, Investigation, Formal analysis. **Junze Zhao:** Software, Formal analysis, Data curation. **Huaming Li:** Supervision, Resources, Project administration. **Jiexiang Xia:** Writing – review & editing, Supervision, Project administration, Funding acquisition. **Bin Wang:** Visualization, Software, Resources. **Yuanbin She:** Writing – review & editing, Supervision, Resources, Funding acquisition.

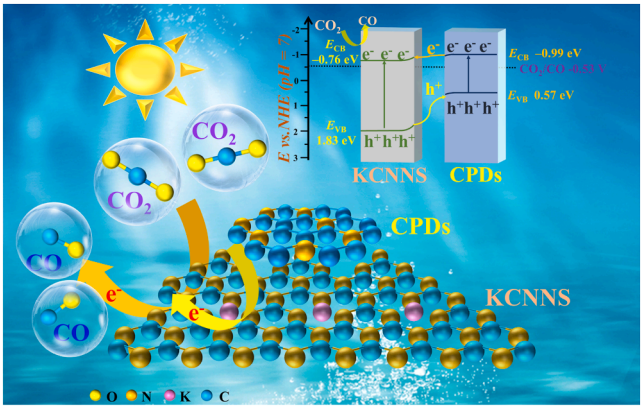

Fig. 10. Schematic band structure of CPDs/KCNNS-2 composites for photocatalytic CO_2 reduction.

Declaration of Competing Interest

The authors declare that they have no known competing financial interests or personal relationships that could have appeared to influence the work reported in this paper.

Data availability

Data will be made available on request.

Acknowledgements

This work was financially supported by National Natural Science Foundation of China (No. 22378172, 22138011), and China Postdoctoral Science Foundation (No. 2022M721380).

Appendix A. Supporting information

Supplementary data associated with this article can be found in the online version at doi:10.1016/j.apcatb.2024.123993.

References

[1] V. Scott, S. Gilfillan, N. Markusson, H. Chalmers, R.S. Haszeldine, Last chance for carbon capture and storage, Nat. Clim. Change 3 (2013) 105–111.
[2] G. Luderer, Z. Vrontisi, C. Bertram, O.Y. Edelenbosch, R.C. Pietzcker, J. Rogelj, H.S. D. Boer, L. Drouet, J. Emmerling, O. Fricko, S. Fujimori, P. Havlík, G. Iyer, K. Keramidas, A. Kitous, M. Pehl, V. Krey, K. Riahi, B. Saveyn, M. Tavoni, D. P. Vuuren, E. Kriegler, Residual fossil CO_2 emissions in 1.5–2 °C pathways, Nat. Clim. Change 8 (2018) 626–633.
[3] R.A. Betts, C.D. Jones, J.R. Knight, R.F. Keeling, J.J. Kennedy, El Niño and a record CO_2 rise, Nat. Clim. Change 6 (2016) 806–810.
[4] H. Chen, H. Dong, Z.Y. Shi, A.K. SenGupta, Direct air capture (DAC) and sequestration of CO_2: dramatic effect of coordinated Cu(II) onto a chelating weak base ion exchanger, Sci. Adv. 9 (2023) eadg1956.
[5] R. Meys, A. Kätelhön, M. Bachmann, B. Winter, C. Zibunas, S. Suh, A. Bardow, Achieving net-zero greenhouse gas emission plastics by a circular carbon economy, Science 374 (2021) 71–76.
[6] H.L. Soest, M.G.J. Elzen, D.P. Vuuren, Net-zero emission targets for major emitting countries consistent with the Paris Agreement, Nat. Commun. 12 (2021) 2140.
[7] A. Velty, A. Corma, Advanced zeolite and ordered mesoporous silica-based catalysts for the conversion of CO_2 to chemicals and fuels, Chem. Soc. Rev. 52 (2023) 1773–1946.
[8] D. Wakerley, S. Lamaison, D. Corral, A. Sarkar, T.F. Jaramillo, M. Fontecave, J. Wicks, E.H. Sargent, A. Clemens, J. Feaster, E.B. Duoss, S. Baker, C. Hahn, S. A. Jaffer, Gas diffusion electrodes, reactor designs and key metrics of low-temperature CO_2 electrolysers, Nat. Energy 7 (2022) 130–143.
[9] B. Wang, X.W. Zhu, F.C. Huang, Y. Quan, G.P. Liu, X.L. Zhang, F.Y. Xiong, C. Huang, M.X. Ji, H.M.M. Li, P.K. Chu, J.X. Xia, Porous edge confinement: high carrier potential and low activation energy barrier synergistically boosting the efficiency of selective photocatalytic CO_2 conversion, Appl. Catal. B 325 (2022) 122304.
[10] B. Wang, H.L. Chen, W. Zhang, H.Y. Liu, Z.K. Zheng, F.C. Huang, J.Y. Liu, G.P. Liu, X.W. Yan, Y.X. Weng, H.M. Li, Y.B. She, P.K. Chu, J.X. Xia, Semimetallic bismuthene with edge-rich dangling bonds: Broad-spectrum-driven and edge-confined electron enhancement boosting CO_2 hydrogenation reduction, Adv. Mater. (2024) 2312676.
[11] J.T. Dong, S.N. Ji, Y. Zhang, M.X. Ji, B. Wang, Y.J. Li, Z.G. Chen, J.X. Xia, H.M. Li, Construction of Z-Scheme MnO_2/BiOBr heterojunction for photocatalytic ciprofloxacin removal and CO_2 reduction, Acta Phys. -Chim. Sin. 39 (2023) 2212011.
[12] Y. Zhang, F.Y. Guo, K.K. Wang, J. Di, B. Min, H.Y. Zhu, H.L. Chen, Y.X. Weng, J. Y. Dai, Y.B. She, J.X. Xia, H.M. Li, Precisely modulate interfacial Bi-O bridge bond in Co-TCPP/Bi_3O_4Br to trigger long-lasting charge separation for boosting CO_2 photoreduction, Chem. Eng. J. 465 (2023) 142663.
[13] Y. Zhang, F.Y. Guo, J. Di, K.K. Wang, M.J. Li, J.Y. Dai, Y.B. She, J.X. Xia, H.M. Li, Strain-induced surface interface dual polarization constructs PML-Cu/$Bi_{12}O_{17}Br_2$ high-density active sites for CO_2 photoreduction, Nano Micro Lett. 16 (2024) 90.
[14] J.R. Ran, M. Jaroniec, S.Z. Qiao, Cocatalysts in semiconductor-based photocatalytic CO_2 reduction: achievements, challenges, and opportunities, Adv. Mater. 30 (2018) 1704649.
[15] L. Yuan, C.Q. Zhang, Y.Y. Zou, T. Bao, J. Wang, C. Tang, A.J. Du, C.Z. Yu, C. Liu, A S-scheme MOF-on-MOF heterostructure, Adv. Funct. Mater. 33 (2023) 2214627.
[16] R. Das, A. Patra, S.K. Dutta, S. Shyamal, N. Pradhan, Facets-directed epitaxially grown lead halide perovskite-sulfobromide nanocrystal heterostructures and their improved photocatalytic activity, J. Am. Chem. Soc. 144 (2022) 18629–18641.
[17] G. Wang, M. Zhang, D. Chen, Q.L. Guo, X.F. Feng, T.C. Niu, X.S. Liu, A. Li, J.W. Lai, D. Sun, Z.M. Liao, Y.Q. Wang, P.K. Chu, G.Q. Ding, X.M. Xie, Z.F. Di, X. Wang, Seamless lateral graphene p–n junctions formed by selective in situ doping for high-performance photodetectors, Nat. Commun. 9 (2018) 5168.
[18] Y.X. Xu, X.L. Jin, T. Ge, H.Q. Xie, R.X. Sun, F.Y. Su, X. Li, L.Q. Ye, Realizing efficient CO_2 photoreduction in Bi_3O_4Cl: Constructing van der Waals heterostructure with g-C_3N_4, Chem. Eng. J. 409 (2021) 128178.
[19] Y. Liu, Y. Huang, X.F. Duan, Van der Waals integration before and beyond two-dimensional materials, Nature 567 (2019) 323–333.
[20] A. Castellanos-Gomez, X.F. Duan, Z. Fei, H.R. Gutierrez, Y. Huang, X.Y. Huang, J. Quereda, Q. Qian, E. Sutter, P. Sutter, Van der Waals heterostructures, Nat. Rev. Methods Prim. 2 (2022) 58.
[21] W.J. Deng, Z.L. Zheng, J.Z. Li, R.K. Zhou, X.Q. Chen, D.H. Zhang, Y. Lu, C. W. Wang, C.Y. You, S.Y. Li, L. Sun, Y. Wu, X.H. Li, B.X. An, Z. Liu, Q.J. Wang, X. F. Duan, Y.Z. Zhang, Electrically tunable two-dimensional heterojunctions for miniaturized near-infrared spectrometers, Nat. Commun. 13 (2022) 4627.
[22] K.K. Paul, J.H. Kim, Y.H. Lee, Hot carrier photovoltaics in van der Waals heterostructures, Nat. Rev. Phys. 3 (2021) 178–192.
[23] P.M. Ismail, S. Ali, S. Ali, J.H. Li, M. Liu, D. Yan, F. Raziq, F. Wahid, G.J. Li, S. H. Yuan, X.Q. Wu, J.B. Yi, J.S. Chen, Q.Y. Wang, L. Zhong, Y. Yang, P.F. Xia, L. Qiao, Photoelectron "bridge" in Van der Waals heterojunction for enhanced photocatalytic CO_2 conversion under visible light, Adv. Mater. 35 (2023) 2303047.
[24] J.P. Wang, Y. Yu, J.Y. Cui, X.R. Li, Y.L. Zhang, C. Wang, X.L. Yu, J.H. Ye, Defective g-C_3N_4/covalent organic framework Van der Waals heterojunction toward highly efficient S-scheme CO_2 photoreduction, Appl. Catal. B 301 (2022) 120814.
[25] J.R. Ran, W.W. Guo, H.L. Wang, B.C. Zhu, J.G. Yu, S.Z. Qiao, Metal-free 2D/2D phosphorene/Van der Waals heterojunction for highly enhanced visible-light photocatalytic H_2 production, Adv. Mater. 30 (2018) 1800128.
[26] H. Liu, S.H. Cao, L. Chen, K. Zhao, C.B. Wang, M.X. Li, S.G. Shen, W.J. Wang, L. Ge, Electron acceptor design for 2D/2D iodinene/carbon nitride heterojunction boosting charge transfer and CO_2 photoreduction, Chem. Eng. J. 433 (2022) 133594.
[27] J.F. Zhang, J.W. Fu, K. Dai, Graphitic carbon nitride/antimonene van der Waals heterostructure with enhanced photocatalytic CO_2 reduction activity, J. Mater. Sci. Technol. 116 (2022) 192–198.
[28] J. Jiang, D.L. Duan, J. Ma, Y.W. Jiang, R. Long, C. Gao, Y.J. Xiong, Van der waals heterostructures by single cobalt sites-anchored graphene and g-C_3N_4 nanosheets for photocatalytic syngas production with tunable CO/H_2 ratio, Appl. Catal. B 295 (2021) 120261.
[29] M. Han, C.Y. Kang, Z.X. Qu a b, S.J. Zhu, B. Yang, Surface molecule induced effective light absorption and charge transfer for H_2 production photocatalysis in a carbonized polymer dots-carbon nitride system, Appl. Catal. B 205 (2022) 121064.
[30] L. Ding, Z.N. Li, R.Y. Liu, Y.F. Li, G.D. Yang, Z.H. Kang, B. Yang, M.X. Deng, H. Z. Sun, Fabrication of electron's path based on carbonized polymer dots to accelerate photocatalytic hydrogen production kinetic for carbon nitride, Appl. Catal. B 334 (2023) 122806.
[31] Y. Zhao, Q.S. Zeng, Y. Yu, T.L. Feng, Y.J. Zhao, Z.D. Wang, Y. Li, C.M. Liu, J.J. Liu, H.T. Wei, S.J. Zhu, Z.H. Kang, H. Zhang, B. Yang, Enhanced charge separation and photocatalytic hydrogen evolution in carbonized-polymer-dot-coupled lead halide perovskites, Mater. Horiz. 7 (2020) 2719–2725.
[32] B. Wang, J.Z. Zhao, H.L. Chen, Y.X. Weng, H. Tang, Z.R. Chen, W.S. Zhu, Y.B. She, J.X. Xia, H.M. Li, Unique Z-scheme carbonized polymer dots/$Bi_4O_5Br_2$ hybrids for efficiently boosting photocatalytic CO_2 reduction, Appl. Catal. B 295 (2021) 120261.
[33] J. Xie, X.J. Zhang, Z.J. Lu, J.D. Hu, A.Z. Hao, Y. Feng, Y.L. Cao, Up-conversion effect boosted the photocatalytic CO_2 reduction activity of Z-scheme CPDs/BiOBr heterojunction, Inorg. Chem. Front. 10 (2023) 5127–5135.
[34] T.Y. Liu, L. Hao, L.Q. Bai, J.G. Liu, Y.H. Zhang, N. Tian, H.W. Huang, Z-scheme junction $Bi_2O_2(NO_3)(OH)$/g-C_3N_4 for promoting CO_2 photoreduction, Chem. Eng. J. 429 (2022) 132268.
[35] Y. Xia, Z.H. Tian, T. Heil, A.Y. Meng, B. Cheng, S.W. Cao, J.G. Yu, M. Antonietti, Highly selective CO_2 capture and its direct photochemical conversion on ordered 2D/1D heterojunctions, Joule 3 (2019) 2792–2805.
[36] J.M. Yang, K.F. Yang, X.W. Zhu, Z.L. Wang, Z.R. Yang, X.D. Ding, K. Zhong, M. Q. He, H.M. Li, H. Xu, Band engineering of non-metal modified polymeric carbon

nitride with broad spectral response for enhancing photocatalytic CO_2 reduction, Chem. Eng. J. 461 (2023) 141841.
[37] W.D. Hou, H.Z. Guo, M.H. Wu, L. Wang, Amide covalent bonding engineering in heterojunction for efficient solar-driven CO_2 reduction, ACS Catal. 17 (2023) 20560–20569.
[38] D.N. Liu, D.Y. Chen, N.J. Li, Q.F. Xu, H. Li, J.H. He, J.M. Lu, Surface engineering of g-C_3N_4 by Stacked BiOBr sheets rich in oxygen vacancies for boosting photocatalytic performance, Angew. Chem. Int. Ed. 59 (2020) 4519–4524.
[39] J.X. Xu, Y.F. Chen, M. Chen, J. Wang, L. Wang, In situ growth strategy synthesis of single-atom nickel/sulfur co-doped g-C_3N_4 for efficient photocatalytic tetracycline degradation and CO_2 reduction, Chem. Eng. J. 442 (2022) 136208.
[40] Y.Y. Duan, Y. Wang, W.X. Zhang, J.W. Zhang, C.G. Ban, D.M. Yu, K. Zhou, J. J. Tang, X. Zhang, X.D. Han, L.Y. Gan, X.P. Tao, X.Y. Zhou, Simultaneous CO_2 and H_2O activation via integrated Cu single atom and N vacancy dual-site for enhanced CO photo-production, Adv. Funct. Mater. 33 (2023) 2301729.
[41] Z. Jiang, X.H. Xu, Y.H. Ma, H.S. Cho, D. Ding, C. Wang, J. Wu, P. Oleynikov, M. Jia, J. Cheng, Y. Zhou, O. Terasaki, T.Y. Peng, L. Zan, H.X. Deng, Filling metal–organic framework mesopores with TiO_2 for CO_2 photoreduction, Nature 586 (2020) 549–554.
[42] G.L. Xu, H.B. Zhang, J. Wei, H. Xia Zhang, X. Wu, Y. Li, C.S. Li, Jian Zhang, J.H. Ye, Integrating the g-C_3N_4 nanosheet with B−H bonding decorated metal−organic framework for CO_2 activation and photoreduction, ACS Nano 12 (2018) 5333–5340.
[43] H. Sun, L. Sun, G.N. Li, Y.X. Tuo, C.L. Ye, J.R. Yang, J.X. Low, X. Yu, J.H. Bitter, Y. P. Lei, D.S. Wang, Y.D. Li, Phosphorus tailors the d-band center of copper atomic sites for efficient CO_2 photoreduction under visible-light irradiation, Angew. Chem. Int. Ed. 61 (2022) e202207677.
[44] S.F. Ji, Y. Qu, T. Wang, Y.J. Chen, G.F. Wang, X. Li, J.C. Dong, Q.Y. Chen, W. Y. Zhang, Z.D. Zhang, S.Y. Liang, R. Yu, Y. Wang, D.S. Wang, Y.D. Li, Rare-earth single erbium atoms for enhanced photocatalytic CO_2 reduction, Angew. Chem. Int. Ed. 59 (2020) 10651–10657.
[45] H.H. Ou, S.B. Ning, P. Zhu, S.H. Chen, A. Han, Q. Kang, Z.F. Hu, J.H. Ye, D. S. Wang, Y.D. Li, Carbon nitride photocatalysts with integrated oxidation and reduction atomic active centers for improved CO_2 conversion, Angew. Chem. Int. Ed. 61 (2021) e202206579.
[46] A.X. Deng, E. Zhao, Q. Li, Y. Sun, Y.Z. Liu, S.G. Yang, H. He, Y. Xu, W. Zhao, H. O. Song, Z. Xu, Z.P. Chen, Atomic cobalt−silver dual-metal sites confined on carbon nitride with synergistic Ag nanoparticles for enhanced CO_2 photoreduction, ACS Nano 17 (2023) 11869–11881.
[47] Y. Li, Q. Yin, Y.S. Zeng, Z. Liu, Hollow spherical biomass derived-carbon dotted with SnS_2/g-C_3N_4 Z-scheme heterojunction for efficient CO_2 photoreduction into CO, Chem. Eng. J. 438 (2022) 135652.
[48] L. Cheng, X.Y. Yue, L.X. Wang, D.N. Zhang, P. Zhang, J.J. Fan, Q.J. Xiang, Dual-single-atom tailoring with bifunctional integration for high-performance CO_2 photoreduction, Adv. Mater. 33 (2021) 2105135.
[49] Z.F. Jiang, W.M. Wan, H.M. Li, S.Q. Yuan, H.J. Zhao, P.K. Wong, A hierarchical Z-Scheme α-Fe_2O_3/g-C_3N_4 hybrid for enhanced photocatalytic CO_2 reduction, Adv. Mater. 30 (2018) 1706108.
[50] Y.Y. Wang, Y. Qu, B.H. Qu, L.L. Bai, Y. Liu, Z.D. Yang, W. Zhang, L.Q. Jing, H.G. Fu, Construction of six-oxygen-coordinated single Ni Sites on g-C_3N_4 with boron-oxo species for photocatalytic water-activation-induced CO_2 reduction, Adv. Mater. 33 (2021) 2105482.
[51] X. Cheng, J.M. Wang, K. Zhao, Y.P. Bi, Spatially confined iron single-atom and potassium ion in carbon nitride toward efficient CO_2 reduction, Appl. Catal. B 316 (2022) 121643.
[52] L. Cheng, P. Zhang, Q.Y. Wen, J.J. Fan, Q.J. Xiang, Copper and platinum dual-single-atoms supported on crystalline graphitic carbon nitride for enhanced photocatalytic CO_2 reduction, Chin. J. Catal. 43 (2022) 451–460.
[53] L. Cheng, H. Yin, C. Cai, J. j Fan, Q.J. Xiang, Single Ni atoms anchored on porous few-layer g-C_3N_4 for photocatalytic CO_2 reduction: the role of edge confinement, Small 16 (2020) 2002411.
[54] J. Tang, X.H. Li, Y.F. Ma, K.Q. Wang, Z.L. Liu, Q.T. Zhang, Boosting exciton dissociation and charge transfer by regulating dielectric constant in polymer carbon nitride for CO_2 photoreduction, Appl. Catal. B 327 (2023) 122417.
[55] Y. Li, B.H. Li, D.N. Zhang, L. Cheng, Q.J. Xiang, Crystalline carbon nitride supported copper single atoms for photocatalytic CO_2 reduction with nearly 100% CO selectivity, ACS Nano 14 (2020) 10552–10561.
[56] J.T. Dong, F. Chen, L. Xu, P.C. Yan, J.C. Qian, Y. Chen, M.Y. Yang, H.N. Li, Fabrication of sensitive photoelectrochemical aptasensor using Ag nanoparticles sensitized bismuth oxyiodide for determination of chloramphenicol, Microchem. J. 178 (2022) 107317.
[57] J.Y. Bai, L.J. Wang, Y.J. Zhang, C.F. Wen, X.L. Wang, H.G. Yang, Carboxyl functionalized graphite carbon nitride for remarkably enhanced photocatalytic hydrogen evolution, Appl. Catal. B 266 (2020) 118590.
[58] W.D. Hou, H.Z. Guo, M.H. Wu, L. Wang, Amide covalent bonding engineering in heterojunction for efficient solar-driven CO_2 reduction, ACS Catal. 17 (2023) 20560–20569.
[59] L.N. Li, Y. Zhang, G.P. Liu, T.G. Wei, J.Z. Zhao, B. Wang, M.X. Ji, Y.B. She, J.X. Xia, H.M. Li, CoTCPP integrates with BiOBr microspheres for improved solar-driven CO_2 reduction performance, Green Energy Environ. DOI: 10.1016/j.gee.2024.01.008.
[60] L.Z. Liu, J.C. Hu, Z.Y. Ma, Z.J. Zhu, B. He, F. Chen, Y. Lu, R. Xu, Y.H. Zhang, T. Y. Ma, M.L. Sui, H.W. Huang, One-dimensional single atom arrays on ferroelectric nanosheets for enhanced CO_2 photoreduction, Nat. Commun. 15 (2024) 305.